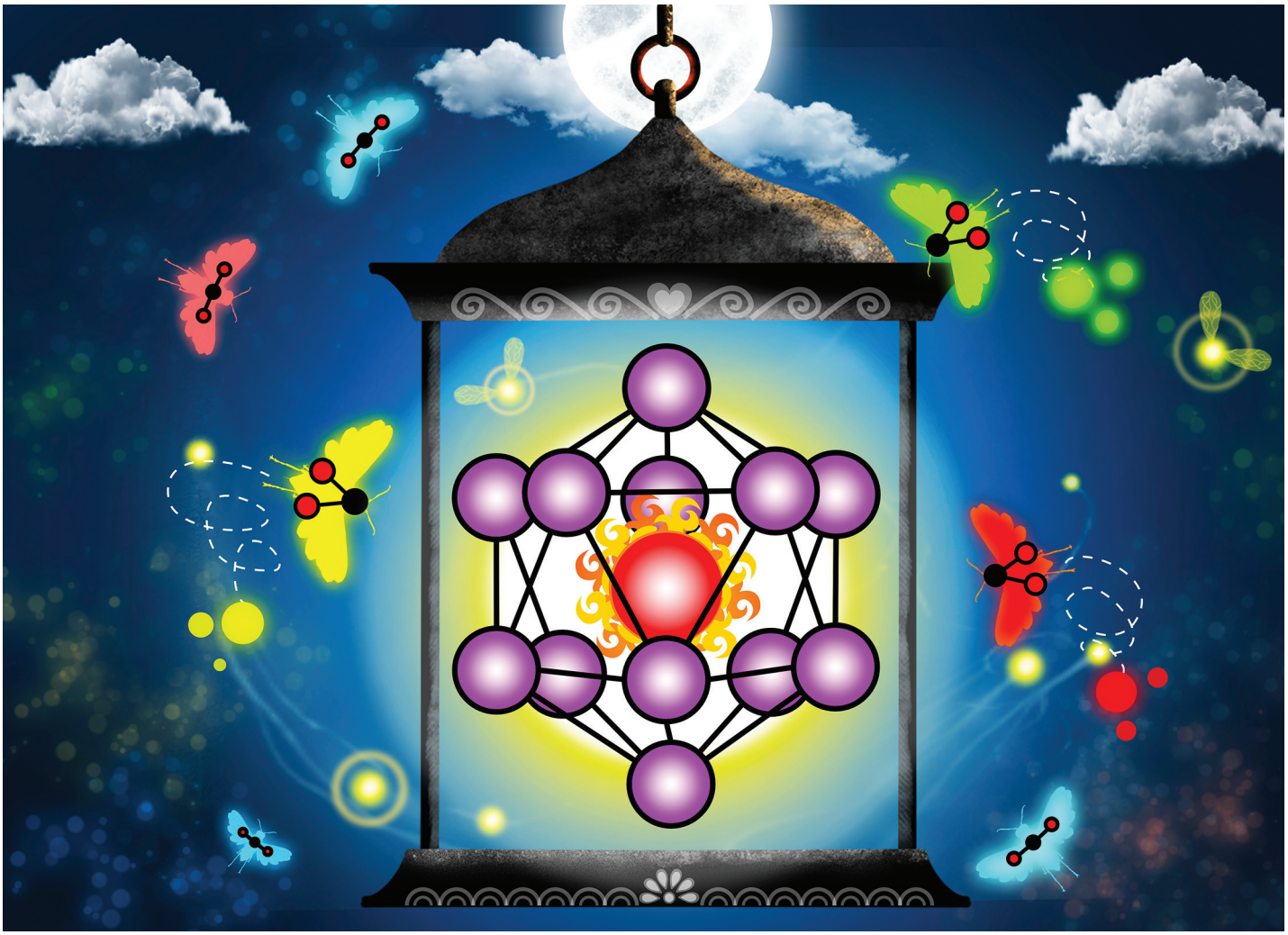

Showcasing research from Professor Puru Jena's group at Physics Department, Virginia Commonwealth University, Richmond, USA.

Activation and electrochemical reduction of carbon dioxide by transition metal atom-doped copper clusters

Transition metal-doped Cu clusters (XCu_{12}, X = 3d/4d elements) significantly enhance CO_2 activation and reduction, addressing Cu's selectivity limitations. Using a multi-scale theoretical approach integrating the Artificial Bee Colony algorithm, extended Tight Binding model, and DFT, stable geometries were determined where X-atoms prefer endohedral positions. These doped clusters exhibit reduced overpotential (~20%) compared to Cu_{13}, offering a promising route to efficient CO_2 electrochemical reduction. An empirical formula derived from DFT data provides further insights, advancing the design of bimetallic catalysts for sustainable chemical conversion.

Image reproduced by permission of Manish Kumar Mohanta from *Nanoscale*, 2025, **17**, 8515.

As featured in:

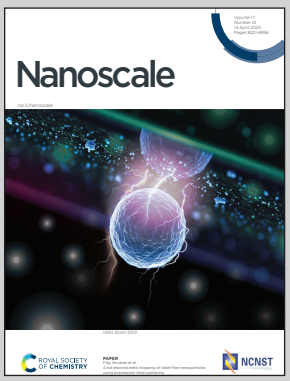

See Manish Kumar Mohanta and Puru Jena, *Nanoscale*, 2025, **17**, 8505.

ROYAL SOCIETY OF CHEMISTRY

rsc.li/nanoscale

Registered charity number: 207890

Nanoscale

ROYAL SOCIETY OF CHEMISTRY

PAPER

View Article Online
View Journal | View Issue

Cite this: *Nanoscale*, 2025, **17**, 8505

Activation and electrochemical reduction of carbon dioxide by transition metal atom-doped copper clusters†

Manish Kumar Mohanta and Puru Jena *

The conversion of CO_2 into valuable chemical products has garnered significant interest due to the pressing need for sustainable solutions. Central to achieving this goal is the development of efficient and cost-effective catalysts. Although Cu is one of the most promising materials for CO_2 reduction, it lacks selectivity. In this study, we explore the effect of doping on the binding affinity and activation of CO_2 by focusing on XCu_{12} clusters, where X represents 3d and 4d transition metal atoms. By employing a multi-scale theoretical approach that integrates the artificial bee colony algorithm, an extended tight binding model, and density functional theory (DFT), the lowest energy geometries of XCu_{12} clusters were determined, revealing that the dopant X-atoms favour endohedral positions, preserving a cage-like structure and maximizing their coordination with the outer Cu-atoms. A thorough analysis of the structural, electronic, and magnetic properties elucidates the varying capabilities of these clusters for the electrochemical reduction of CO_2 to CO. Doping of transition metal atoms is found to significantly modify the electronic and magnetic properties of the clusters, enhancing their reactivity towards CO_2. A significant reduction of about 20% in overpotential for CO_2 reduction is observed in doped clusters compared to the pure Cu_{13} cluster. An empirical formula is proposed by fitting the DFT data using ordinary least squares (OLS) regression. This comprehensive study provides fundamental insights into the potential of bimetallic copper clusters for CO_2 activation and reduction, emphasizing their role in advancing catalytic processes for sustainable chemical production.

Received 15th September 2024,
Accepted 4th February 2025

DOI: 10.1039/d4nr03795b

rsc.li/nanoscale

1. Introduction

An increase in CO_2 concentration in the environment due to the use of fossil fuels is an existential threat to society. Considerable efforts are being made to develop technologies not only for minimizing the emission of CO_2 but also for its capture, sequestration, and conversion to useful chemicals such as formic acid, carbon monoxide, ethanol, and other value-added products.[1,2] Because CO_2 is an extremely stable molecule that not only requires 750 kJ mol^{-1} energy for dissociation but also involves a multielectron process,[3] converting it into useful chemicals is a challenging task; the first step is to bind, activate, and dissociate it at a low energy cost.[4,5]

Copper is found to be one of the best candidates that can reduce CO_2 to more than thirty different hydrocarbons and oxygenates.[6–8] Hence, research on electrochemical reduction of CO_2 (eCO_2R) is primarily focused on Cu-based surfaces. However, it lacks selectivity. The faradaic efficiency for ethylene formation on polyamine-incorporated Cu electrode[9] does not surpass 40% at a current density 200 mA cm^{-2}. Experimental studies on the catalytic performance of Al_2O_3-supported copper nanoclusters (n = 3, 4, 20) in CO_2 hydrogenation to methanol have shown that catalytic efficiency is greatly influenced by cluster size. Among the tested catalysts, Cu_4/Al_2O_3 exhibited the highest activity, while Cu_3/Al_2O_3, with one fewer copper atom, showed a significant drop in performance, deviating from the size-dependence trend seen in gas-phase clusters.[10–12] The ligated metal nanoclusters have also demonstrated enhanced electrocatalytic activity for CO_2 reduction.[13–15] Recent studies have highlighted the unique electronic and catalytic behaviour of size-selected subnanometer transition metal clusters, setting them apart from metal surfaces and larger nanoparticle systems.[16–18] Recent experimental findings have demonstrated the efficient formation of C_2 products on small copper clusters incorporated into mesoporous carbon spheres, metal–organic frameworks or copper coordination polymers.[19–23]

Recent efforts focus on identifying new active sites and probing the activation mechanism theoretically.[24–29] Atomic

Department of Physics, Virginia Commonwealth University, Richmond, Virginia 23284, USA. E-mail: pjena@vcu.edu

† Electronic supplementary information (ESI) available. See DOI: https://doi.org/10.1039/d4nr03795b

clusters offer an added advantage not only because most of the atoms are surface atoms but also because the surface topology is very different from the planar surface. Past DFT studies have shown that small copper clusters (Cu_4) are excellent candidates for the activation of CO_2 molecules.[30,31] This work instead focuses on the icosahedral Cu_{13} cluster as an ideal platform where all the surface atoms are equivalent by symmetry. In addition, the electronic structure of Cu_{13} cluster can be further modified by doping where one of the Cu atoms is replaced by either a 3d (Sc, Ti, V, Cr, Mn, Fe, Co, Ni, Zn) or a 4d (Y, Zr, Nb, Mo, Tc, Ru, Rh, Pd, Ag, Cd) transition metal atom, X. Note that the number of outer electrons of 3d and 4d transition metal atoms vary from 3 in Sc (Y) to 12 in Zn (Cd). With each Cu atom contributing one electron to the valence pool, the total number of electrons taking an active part in a chemical reaction varies from 15 in $ScCu_{12}$ (YCu_{12}) to 24 in $ZnCu_{12}$($CdCu_{12}$). In addition, the magnetic moments of the transition metal atoms also vary across the 3d and 4d series with Zn and Cd having no unpaired spins and each Cr and Mo atom having the largest magnetic moment of 6 μ_B. Interestingly, Cu_{13}, $AgCu_{12}$, and $ZnCu_{12}$ clusters composed entirely of non-magnetic elements are found to possess large magnetic moments. Recent experiments have led to the successful synthesis of atomically precise copper-rich bimetallic superatom clusters.[32]

The influence of the electronic and magnetic structure on CO_2 binding and activation is systematically explored by doping transition metal (TM) atoms, X, into the Cu_{13} cluster, forming XCu_{12} bimetallic clusters. To calculate the overpotential in the electrochemical CO_2 reduction reaction (CO_2RR), we focused exclusively on 3d-atom doped XCu_{12} clusters, specifically Cr/Mn/Fe/Co/Ni/Cu-Cu_{12}. We aim to establish a connection between the properties of these doped clusters and their effect on CO_2RR performance.

2. Computational details

The first step in our calculation is to determine the equilibrium geometry of XCu_{12} clusters (X = any of the 3d or 4d atoms). Note that the Cu_{13} cluster is icosahedral with the central atom surrounded by 12 surface atoms. When an X atom is used to replace a Cu atom, it can either occupy the interior site of the icosahedron or one of the surface sites. We used the Artificial Bee Colony (ABC) algorithm implemented in the ABCluster program to classify initial global minimum energy conformation/structure (GMEC).[33,34] The ABC algorithm combined with eXtended tight binding (denoted as ABC-*x*TB) was found to be an effective approach to evaluating GMEC with the accuracy of the first-principle method. The initial structures obtained from the ABC-*x*TB calculations were further optimized using spin unrestricted density functional theory (DFT) with hybrid exchange–correlation potential, B3LYP (Becke 3-parameter Lee–Yang–Parr hybrid functional)[35,36] and the def2-TZVP basis set[37] implemented in the Gaussian16 package.[38] The effect of van der Waals interaction on the chemisorption of CO_2 molecule is incorporated using Grimme's D3 dispersion scheme.[36,39] We have considered all possible spin multiplicities for each geometry to ensure the robustness of the ground-state search. Further, vibrational-frequency analysis ensures that a single imaginary frequency corresponds to the transition state. The spin population analysis is carried out using the Multiwfn program.[40] The CO_2 reduction calculation is performed using the Vienna *ab initio* simulation package (VASP) details of which are provided in the ESI.†[41–44]

3. Results and discussion

3.1 Geometry, stability, electronic, and magnetic properties of transition metal-doped XCu_{12} bimetallic neutral clusters

As an example of the search of the phase space carried out by using the ABCluster algorithm without any symmetry constraint, we present a list of initial structures sorted by energy for $CrCu_{12}$ in Fig. 1(a). These were further optimized using DFT. The surface site occupancy of the dopant was found to be 10.3 eV higher than the central site occupancy in the case of $CrCu_{12}$ as indicated in Fig. 1(b). In all cases, we found that the TM atoms, X, occupy the central site, maintaining a cage structure and maximizing their coordination with the surface Cu atoms. All clusters are found to be dynamically stable with no imaginary frequencies. The coordinates of a few selected atoms can be found in ref. 45. Only four clusters (*e.g.*, Cu_{13}, $CrCu_{12}$, $MoCu_{12}$, and $AgCu_{12}$) are found to retain perfect icosahedral symmetry. Among these, Cu_{13} and $AgCu_{12}$ clusters are isoelectronic while $CrCu_{12}$ and $MoCu_{12}$ clusters adhere to the 18-electron shell closure rule. For small clusters such as Sn-doped Cu_4 clusters studied by Tommaso *et al.*,[46] the catalytic reaction occurs at a new active site Sn which is different from this work.[47] In all XCu_{12} clusters, only the Cu atoms are exposed to catalytic reaction, making it easy to study the effect of doping on CO_2 binding and activation.

Now, to understand the influence of transition metal atoms on the stability of XCu_{12} clusters, the substitutional doping energy for a single dopant atom X in the Cu_{13} cluster is calculated using the following equation.[48]

$$E_{sub} = \frac{1}{13}[E_{XCu_{12}} + E_{Cu} - E_{Cu_{13}} - E_X] \quad (1)$$

Here, E(X), E(Cu) and E(XCu_{12}, Cu_{13}) represent the total energies of transition metal atoms, copper atoms, and XCu_{12} and Cu_{13} clusters, respectively. The positive E_{sub} value indicates that the substitution process is endothermic and hence unfavourable. The results are plotted in Fig. 1(c). Among the 3d- and 4d-series, $CrCu_{12}$ and $MoCu_{12}$ clusters, respectively, are found to be the most stable structures due to the 18-electron shell closure rule while $ZnCu_{12}$, $AgCu_{12}$, and $CdCu_{12}$ clusters are less stable than the Cu_{13} cluster.

The vertical ionization potentials (IP) are calculated using the following equation.

$$IP = E_{tot}(N-1) - E_{tot}(N) \quad (2)$$

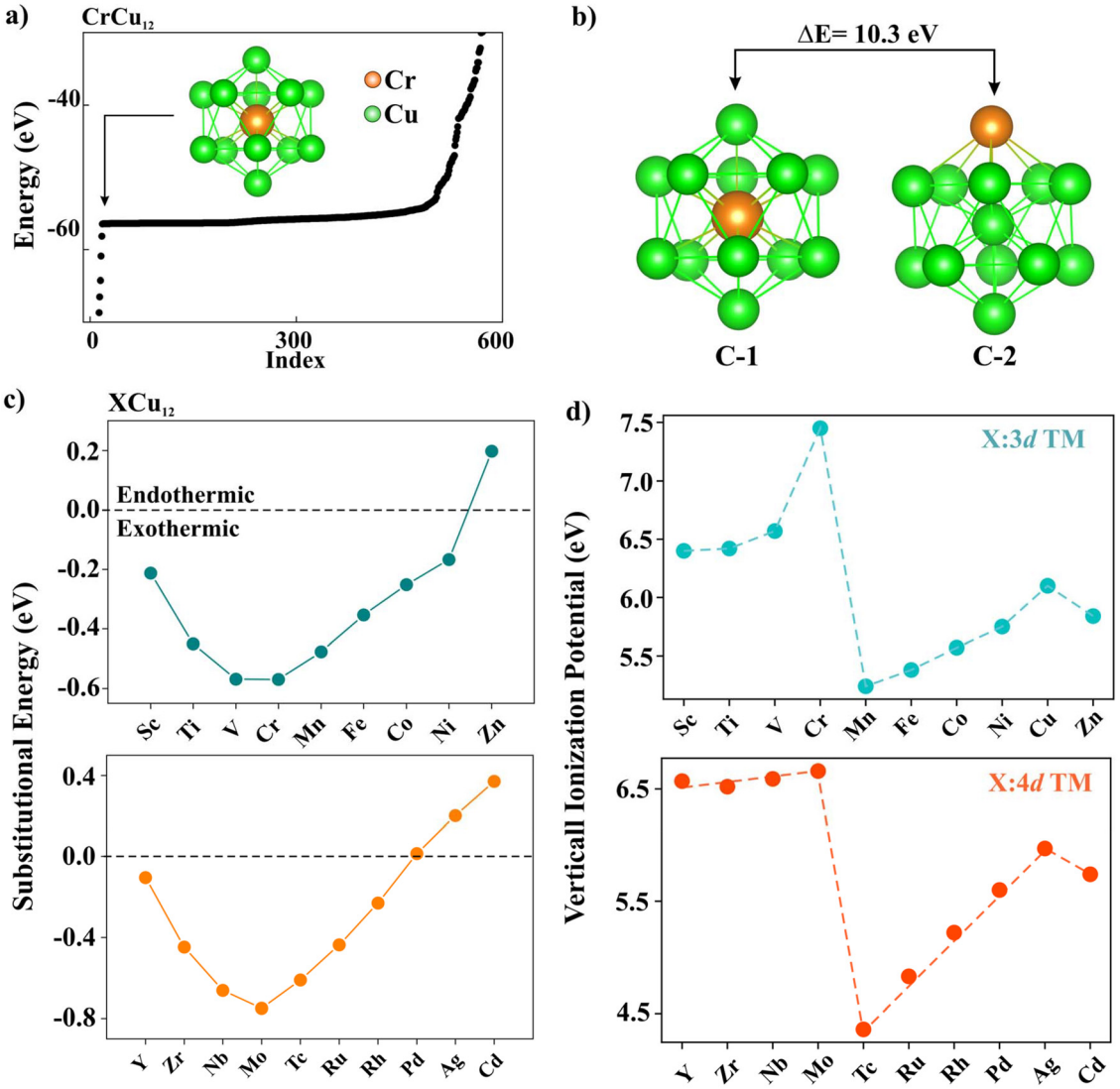

Fig. 1 (a) Guess structures of $CrCu_{12}$ cluster sorted by their energy; (b) energy difference between its two different configurations, cluster C-1 where Cr is positioned at the centre of the icosahedral and C-2 where Cr is positioned at the surface site; (c) substitutional energy and (d) vertical ionization potential of all the transition metal atom-doped clusters.

where N is the number of electrons of the neutral cluster and $E_{tot}(N)$ is its total energy. The results are presented in Fig. 1(d). A significant drop in the IP is evident at $MnCu_{12}$ and $TcCu_{12}$, which is attributed to the elevated IPs of $CrCu_{12}$ and $MoCu_{12}$ clusters in the 3d and 4d series, in line with the 18-electron shell closure rule.

The highest occupied molecular orbital (HOMO) and the lowest unoccupied molecular orbital (LUMO) of the Cr/Mn/Fe/Co/Ni/Cu-Cu_{12} clusters are plotted in Fig. 2 for a systematic comparison. Note that the MOs of the Cr atom are consistent with it being found in a "spherically symmetric" potential well with orbital occupancy as $1s^2 1p^6 1d^{10} 2s^2$. A notable decrease in the HOMO–LUMO gap, ranging from 2.72 eV to approximately 0.9 eV, is observed when Cu is substituted by various transition metals (TM), highlighting the impact of dopants on electronic properties. Fig. 2 highlights the shift in the relative contributions of various molecular orbitals to both the HOMO and LUMO. Fig. S1† depicts the distribution of percentage contributions from transition metal (X) atoms in the HOMO and LUMO, showing that Cu contributes about 75% to the HOMO, whereas transition metal atoms account for nearly 80% of the LUMO.[49] Fig. S2† displays the molecular surface map of the average local ionization energy ($\bar{I}$), revealing that the outer Cu atoms are the most favourable sites for electrophilic attack, playing a crucial role in cluster–molecule interactions.

3.2 Magnetic properties of transition metal-doped XCu_{12} bimetallic clusters

The 3d and 4d elements have partially filled d-shells, leading to magnetic moments that vary based on the number of elec-

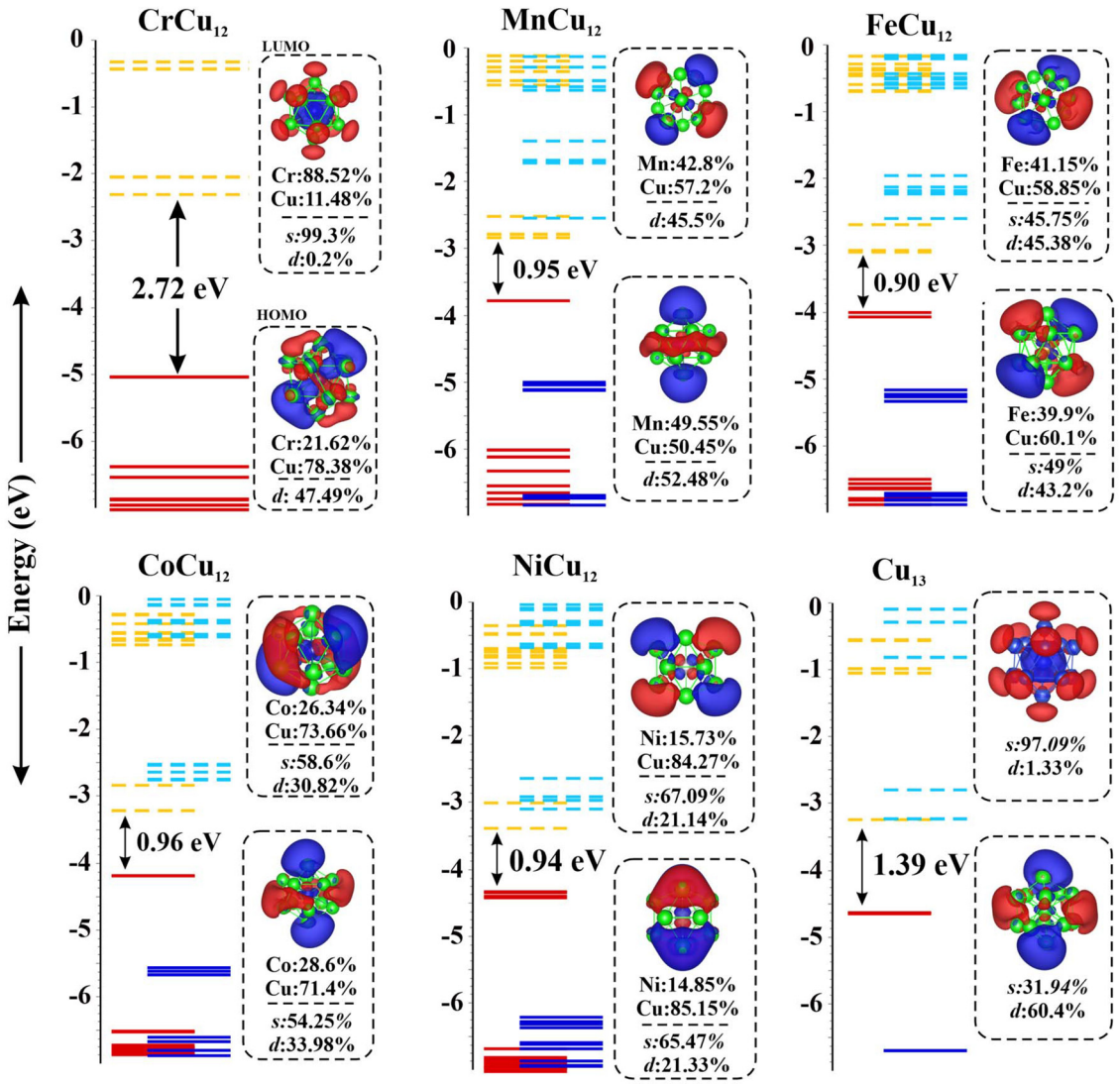

Fig. 2 Molecular orbital maps of HOMO and LUMO of the Cr/Mn/Fe/Co/Ni/Cu-Cu_{12} clusters; solid and dashed lines represent occupied and unoccupied states.

trons in the d-orbitals. These values are illustrated in Fig. S2(b).† They range from $1\mu_B$ in Sc (Y), peak at $6\mu_B$ in Cr (Mo), and diminish to zero in Zn (Cd). When the transition metal atoms are doped into the copper cluster, the unpaired d-electrons contribute to the copper cluster, modifying the net spin magnetic moment. To determine the preferred magnetic moments of XCu_{12} clusters, we calculated the total energies for various spin multiplicities with the findings summarized in Table S1.† Fig. S2(b)† compares the total preferred magnetic moments of all clusters with those of isolated 3d and 4d transition metal atoms. Notably, the magnetic moments decrease from $ScCu_{12}$ (YCu_{12}) to $CrCu_{12}$ ($MoCu_{12}$) where they are completely quenched following the 18-electron shell-closure rule. The magnetic moments then increase, reaching a maximum at Cu_{13} ($AgCu_{12}$), exhibiting a magnetic moment of $5\mu_B$. Interestingly clusters like Cu_{13}, $AgCu_{12}$, and $ZnCu_{12}$ are composed of non-magnetic elements, yet they show significant magnetic moments. Among the transition metals studied, Ti/Zr and Co/Rh uniquely retain their atomic magnetic moment when embedded in the Cu_{13} cluster.

3.3 Adsorption and activation of CO_2 on XCu_{12} clusters

To catalytically convert CO_2, the first critical step is to examine its adsorption on the catalyst surface, distinguishing between physisorption and chemisorption and evaluating the molecule's activation level. In the physisorbed state, CO_2 maintains its gas phase geometry with a C–O bond length of 1.18 Å and an O–C–O bond angle of 180°. In contrast, chemisorption results in elongated C–O bonds and a loss of linearity, with the linear O═C═O becoming bent signifying the activation of the CO_2 molecule.

The effect of the surface topology on the adsorption of CO_2 is studied by focusing on a flat Cu (111) surface, Cu_{13}, Cu_{18}, and Cu_{24} clusters. Our choice of Cu_{18}, Cu_{24} clusters was

motivated by the fact that their geometries are available on the database.[50] The resulting geometries with interacting CO_2 are given in Fig. S3.† The CO_2 molecule interacts differently as seen from the change in bond length and bond angle. It is weakly bound at a distance of 3.1 Å from the Cu (111) surface with a C–O bond length of 1.17 Å and ∠OCO bond angle of 178.9°, remaining close to their pristine gas-phase values of 180° and 1.18 Å, respectively. The binding energy of CO_2 on the Cu (111) surface, as defined in eqn (3), is 0.21 eV. In contrast, the CO_2 binding energy on the Cu_{13} cluster is significantly higher, reaching 2.18 eV. In addition, the CO_2 undergoes significant bending with ∠OCO bond angle of 134.9° and ~8.7% bond elongation (1.28 Å), reflecting the effect of the surface morphology of the Cu-cluster. In an earlier study on cobalt porphyrin nanotubes, Sun and coworkers[51] also observed the effect of surface morphology on chemical reactions. A comparative plot of CO_2 chemisorption on a larger copper cluster is shown in Fig. S3.† While surface morphology significantly influences CO_2 activation, this study primarily focuses on the effects of doping.

Our subsequent study focused on the interaction between CO_2 and the XCu_{12} clusters. In Fig. 3, we present the optimized geometries of a few clusters. Notably, even though $CrCu_{12}$ is an electronically close-shell system, the ∠OCO bond angle of 136.6° indicates its potential for CO_2 activation. The binding energies ($E_{b\_CO_2}$) of CO_2 is calculated using eqn (3).

$$E_{b\_CO_2} = [E_{XCu_{12}CO_2} - E_{XCu_{12}} - E_{CO_2}] \quad (3)$$

Here, $E_{XCu_{12}CO_2}$ is the energy of the fully optimized structure of $XCu_{12}CO_2$ and $E_{XCu_{12}}$ and E_{CO_2} are energies of the XCu_{12} cluster and CO_2 molecule, respectively. Positive binding energy indicates a favorable binding of the CO_2 to the metal cluster. The results are plotted in Fig. 4(a) while ∠OCO angles and C–O bond lengths of CO_2 adsorbed on XCu_{12} clusters are summarised in Table S2 of the ESI.† The interaction strength diminishes with an increasing number of valence electrons, hitting a low point for $CrCu_{12}$ (1.37 eV) and $MoCu_{12}$ (1.17 eV) before rising again. This is a reflection of the closed 18-electron shell configuration. Variations in the interaction between clusters and CO_2 molecules are evident in the bending of the ∠OCO bond angle and the elongation of the C–O bond. Fig. 4(b) illustrates these effects. Specifically, greater binding energies correlate with increased deformation of both the C–O bond length and ∠OCO bond angle. Considering a bending angle of 130 degrees and 10% bond elongation as a reference (refer to Fig. 4(b)), only a few clusters show strong activation capabilities of CO_2 molecules out of 18 clusters highlighted with colored backgrounds. The physical stretching and bending of CO_2 can be characterized by charge transfer from the cluster to the CO_2 molecule, polarizability and many more properties of the cluster. The highlighted clusters in Fig. 4(b) have comparatively lower IP (refer to Fig. 1(d)), which indicates easy transfer of electronic charge to CO_2, resulting in higher bending. The Mulliken charge analysis confirms that the CO_2 molecule acquires a significant amount of charge after getting adsorbed on the Cu cluster. Table S2† presents the charge transfer values to CO_2, with Fig. S4† illustrating that, among both the 3d and 4d series clusters, $CrCu_{12}$ and $MoCu_{12}$ exhibit the minimum charge transfer to CO_2, adhering to the 18-electron closed-shell rule. Some of the previously reported Cu-based and other clusters are shown to activate CO_2, such as Cu_2Sn_2 (132.7°, 8.5%),[46] $[B_{12}(CN)_{11}]^{2-}$ (127°, 0.8%),[52] $CuZr_3$

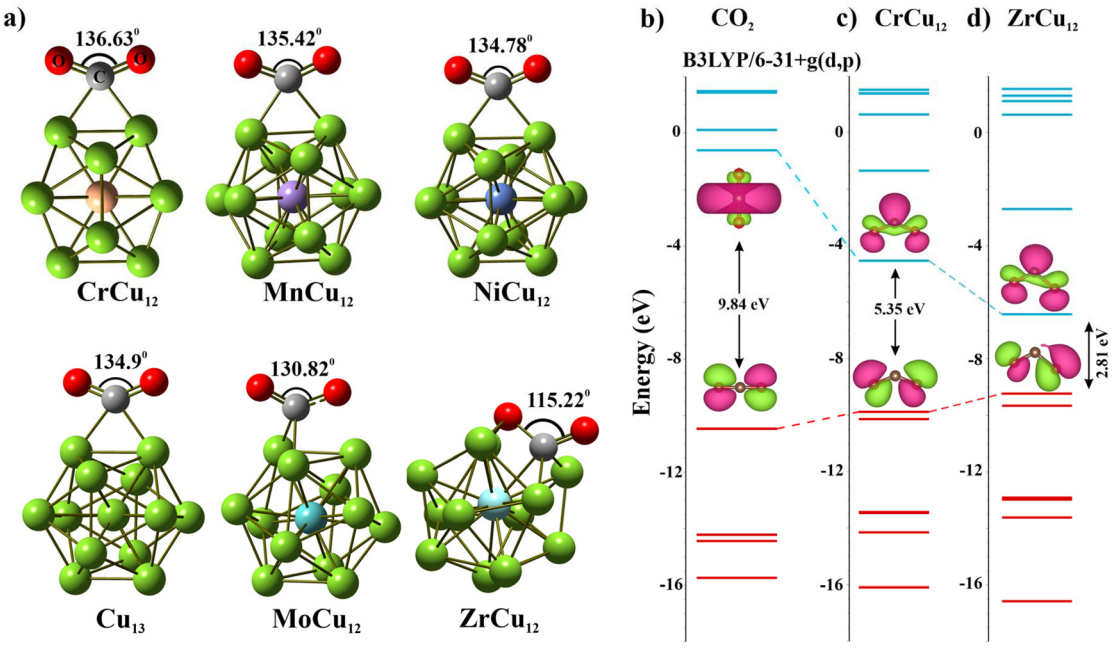

Fig. 3 (a) CO_2 adsorption on various clusters demonstrates varying degrees of chemisorption, evolution of HOMO–LUMO MO energies of different CO_2 configurations obtained from (b) unperturbed CO_2, (c and d) Cr/$ZrCu_{12}$ cluster.

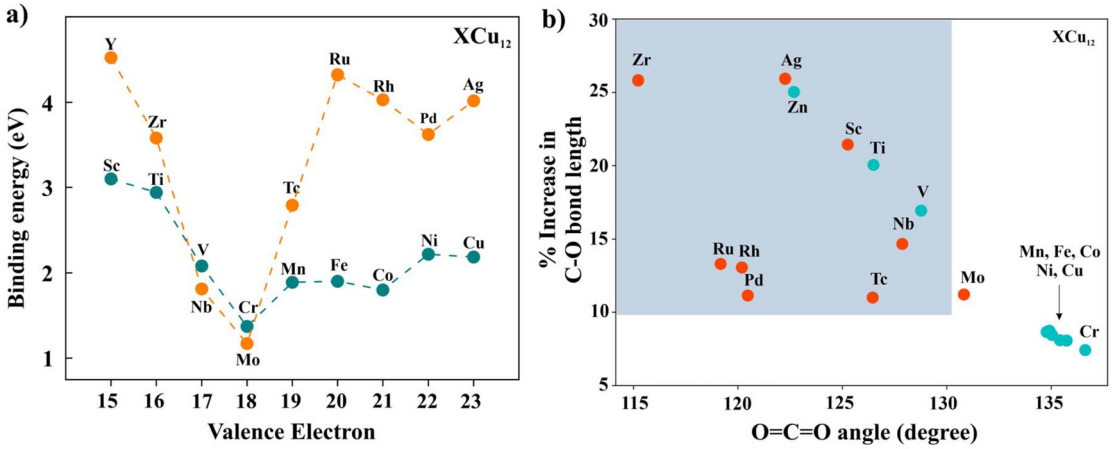

Fig. 4 (a) Binding energy of the CO_2 in different clusters, (b) bond angle (∠OCO) and percentage increase in bond length of CO_2 after chemisorption on the clusters; bond length of C–O (1.18 Å) in gaseous CO_2 molecule is used as a reference.

(115.6°, 16.9%).[53] Considerable bending of the CO_2 molecule is observed in all the clusters while maximum bond length elongation (C═O to C–O) can be observed in the $ZrCu_{12}$ cluster. The evolution of the MO energy diagram of CO_2 in the unperturbed and chemisorbed state on different clusters is provided in Fig. 3. The uneven distribution of molecular orbitals can be depicted as the bending angle varies.

The polarizability of neutral clusters is one of the main descriptors of intermolecular force in physisorbed systems. The average polarizabilities of each cluster in the equilibrium configuration are calculated as,

$$\tilde{\alpha} = \frac{1}{3}(\alpha_{xx} + \alpha_{yy} + \alpha_{zz}), \quad (4)$$

where α_{xx}, α_{yy} and α_{zz} are elements of the polarizability tensor. The variation of the polarizability of the TM-doped clusters is plotted in Fig. 5 where group-2 (X = 4d atoms) clusters exhibit greater polarizability compared to group-1 (X = 3d atoms).

For a systematic comparison, the calculated data for group-1 and group-2 clusters are plotted in Fig. 5. The wider section of the violin plot represents a higher probability whereas the narrower sections represent a lower probability. From Fig. 5(a), the median bending angle for group 1 is ~135° whereas that for group 2 it is ~120°. The binding energies as well as the polarizabilities of the group-2 clusters are much higher than that of the group-1 clusters which indicates better activating properties of the former. Further, to investigate the dependence between multiple properties of clusters, a correlation matrix that measures the linear correlation is constructed from both group-1 and group-2 data sets. The results are given in Fig. 5(d). From this Pearson correlation matrix, the bending angle and bond elongation are highly correlated with the binding energy, charge transfer, and polarizability of the cluster whereas other parameters such as ionization potential, and number of valence electrons are found to be less correlated. The reason lies in the behaviour of the plots similar to a function $|x|$ which has both positive and negative coefficients as can be seen in Fig. 4(a). To elucidate this point, we have divided the data into two sets; (i) 16 to 18 valence electrons and (ii) 19–24 valence electrons, with the results depicted in Fig. 5(e) and Fig. S5.† The correlation matrix indicates that all parameters are linearly correlated with each other.

3.3 Electrocatalytic CO_2 reduction reaction (CO_2RR) on clusters

The CO_2RR involves multiple proton and electron transfer processes. This section systematically investigates the electrochemical conversion of CO_2 to CO on the Cr/Mn/Fe/Co/Ni/Cu-Cu_{12} clusters. The reaction process involved different intermediate steps described as;[29,54]

$$CO_2\ (g) + * \rightarrow *CO_2 \quad (5)$$

$$*CO_2 + (H^+ + e^-) \rightarrow *COOH \quad (6)$$

$$*COOH + (H^+ + e^-) \rightarrow *CO + H_2O\ (g) \quad (7)$$

$$*CO \rightarrow * + CO\ (g) \quad (8)$$

The reduction process of CO_2 in the adsorbed state to CO follows three key reaction steps. The first two steps involve protonation and charge transfer between the adsorbed CO_2 and a free hydrogen atom in the environment, resulting in the formation of the *COOH intermediate which further undergoes a protonated charge transfer process to yield the desired products, *CO and H_2O. Finally, the adsorbed *CO product desorbs from the surface in the third reaction step.

To quantify these intermediate processes, the Gibbs free energy change (ΔG) for each intermediate can be evaluated by the computational hydrogen electrode (CHE) model given as;[55,56]

$$\Delta G = \Delta E_{DFT} + \Delta E_{ZPE} - T\Delta S - eU \quad (9)$$

where ΔE_{DFT}, ΔE_{ZPE} and ΔS signify the differences in the total DFT energy, zero-point energy, and entropy, respectively. U represents the applied potential which is set to zero. The maximum Gibbs free-energy change (ΔG_{max}) can characterize the rate-determining step (RDS) of the complete CO_2RR

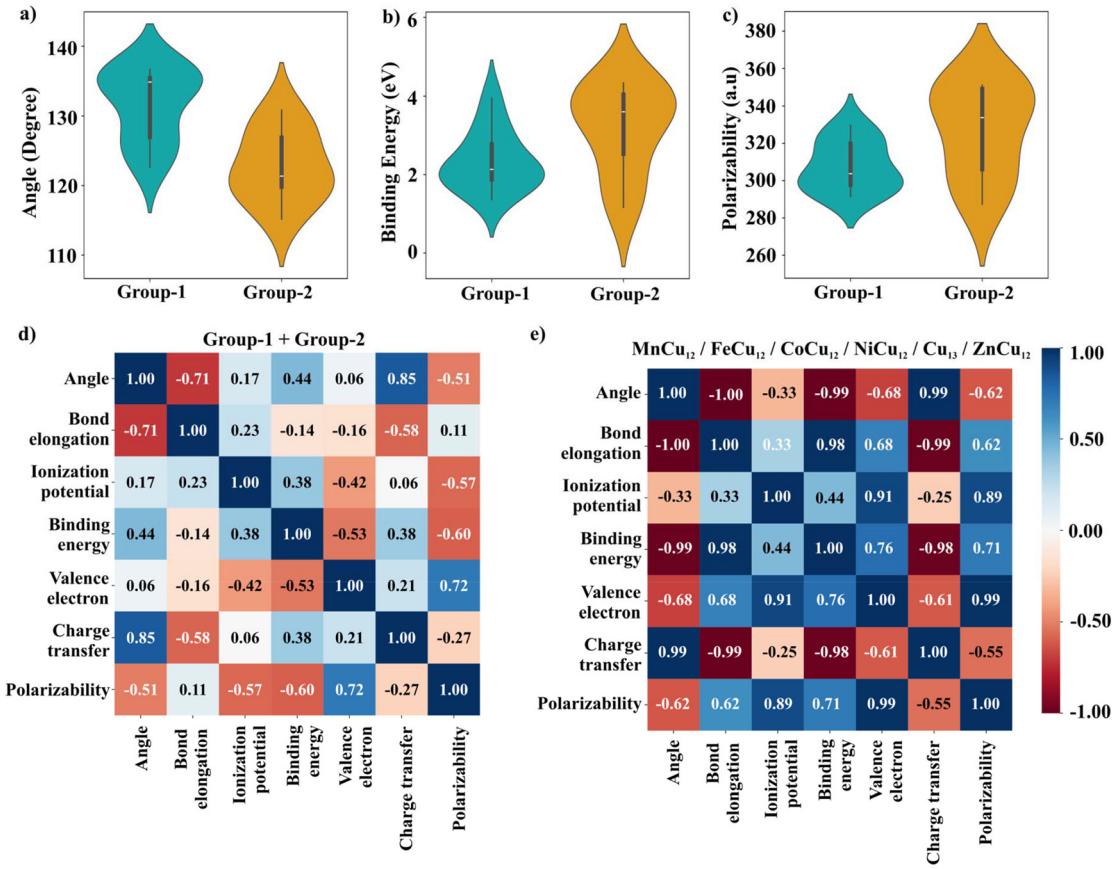

Fig. 5 Violin plot of (a) bond angle of CO_2 in the chemisorbed state, (b) binding energy of CO_2 (c) polarizability of TM-doped cluster, (d–e) Pearson correlation plot; angle refers to O═C═O bond angle.

process. The overpotential (η) is a crucial metric for catalytic performance and is quantitatively equivalent to the limiting potential;

$$\eta = -U_L = \Delta G_{max}/e \quad (10)$$

Here U_L denotes the electric potential required to surpass the energy barrier of the potential-limiting step. Using Gibb's free energy change (ΔG) method, the CO_2 reduction to CO on Cr/Mn/Fe/Co/Ni/Cu-Cu_{12} clusters is first investigated with the results displayed in Fig. 6. As observed in Fig. 6(a), the RDS for all clusters occurs at the third step, *CO → * + CO (g), with energy barriers of 1.33, 1.42, 1.50, 1.57, 1.65, and 1.72 eV respectively. Notably, the overpotential and the magnetic moments of the clusters follow a similar trend, as depicted in Fig. 6(b). Finally, the competitive reaction to form H_2 is also examined, given that CO_2 reduction typically occurs in a liquid environment. To assess this possibility, the initial step of hydrogenation leading to potential intermediates such as *COOH is evaluated using the BrØnsted–Evans–Polanyi (BEP) relation, which is derived from the change in Gibb's free energy. The free energy profile of hydrogen atom adsorption is plotted in Fig. 6(c) and the selectivity plot is presented in Fig. 6(d).[57] It is important to note that the upper (left) and lower (right) regions represent the selectivity for HER and CO_2RR products, respectively. In this study, for most of the clusters with the exception of $CrCu_{12}$, the intermediate *COOH is more likely to form due to its lower ΔG value. It is interesting to note that the calculated adsorption energies of water on the clusters 0.4–0.7 eV (refer to Table S4†) are close to or slightly higher than the experimental value of water adsorption on Cu(110) surface[58] (10 kcal mol^{-1} = 0.43 eV). The adsorption energy of the water molecule is 0.42 eV for the Cu_7 cluster.[59]

Identifying an intrinsic descriptor with predictive power, independent of further DFT calculations, is crucial for efficiently screening the best catalysts from a vast array of material candidates. In this context, to establish a relationship with the overpotential (η^{CO}) for TM-doped clusters, a straightforward yet fundamental descriptor (Φ) can be used which is defined by:[60,61]

$$\Phi = \frac{N}{r_{TM} \times n} \quad (11)$$

where N, r_{TM} and n are the number of d electrons, atomic radius, and periodic number of TMs (see Table S4†). The variation and Pearson correlation matrix of DFT obtained cluster parameters such as the magnetic moment of the cluster, an inherent descriptor of dopant TM, and polarizability is plotted in Fig. 7(a and b).

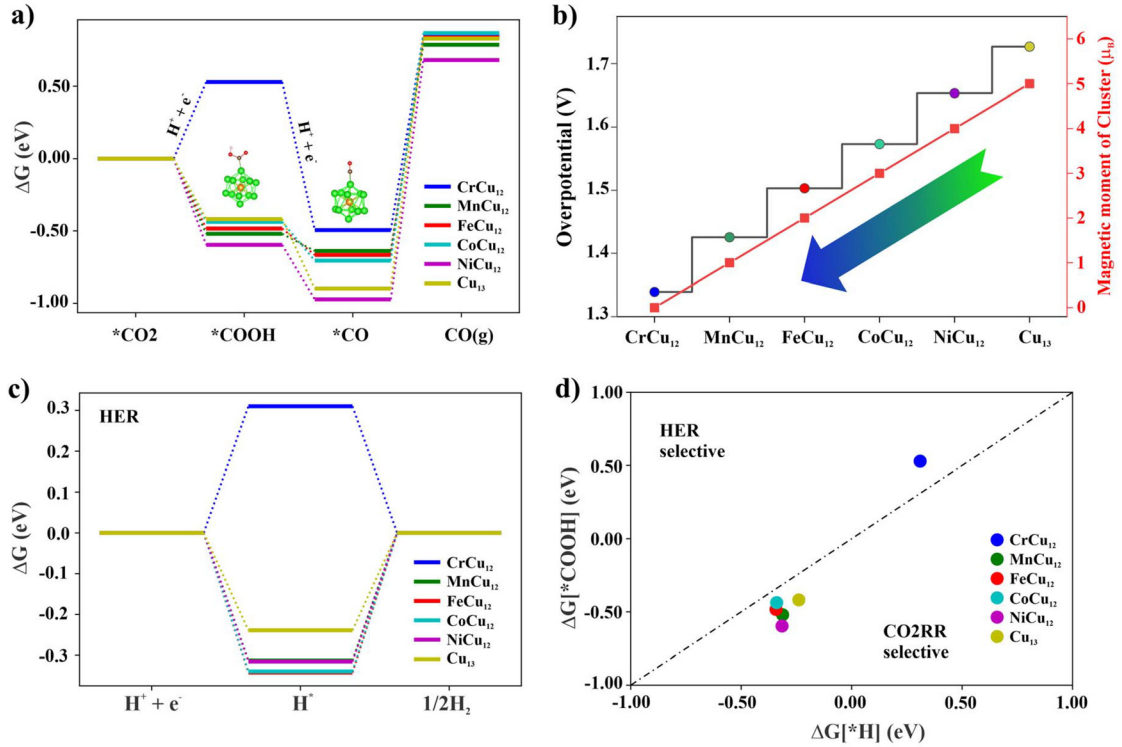

Fig. 6 (a) The free-energy change profile of CO_2 reduction to CO on XCu_{12} clusters, (b) the overpotential of CO_2 reduction, (c) the free-energy profile of hydrogen adsorption, and (d) the selectivity plot between CO_2RR and HER. Clusters below the dotted lines are expected to exhibit the CO_2RR selectivity.

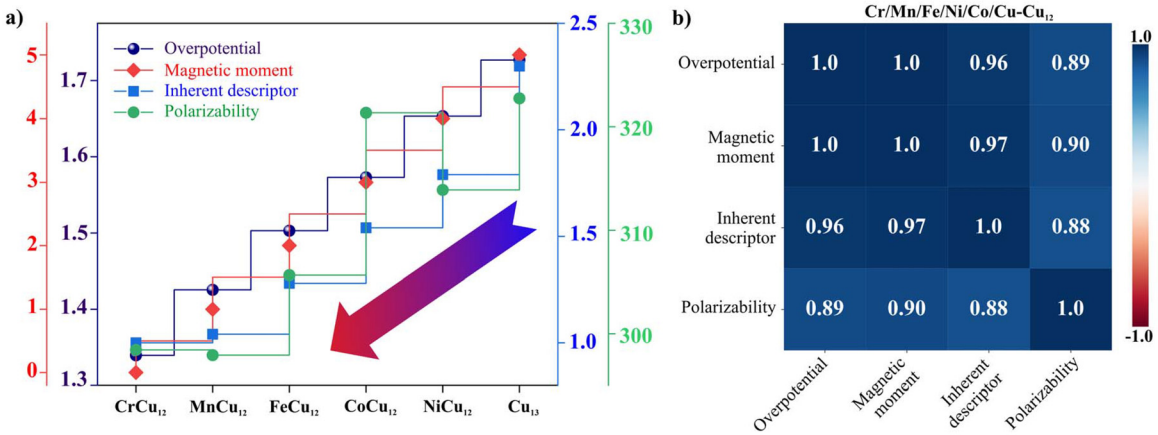

Fig. 7 (a and b) Variation of different cluster parameters and their Pearson correlation plot.

Now considering overpotential as a dependent variable and the other three as independent variables, a relationship can be obtained by fitting the DFT obtained data with the ordinary least squares (OLS) regression method. This is given by;

$$\begin{aligned}\text{Overpotential} = {} & C_0 + C_1 \times \text{magnetic moment} \\ & + C_2 \times \text{inherent descriptor} \\ & + C_3 \times \text{polarizability}\end{aligned} \quad (12)$$

where the coefficients are found to be $C_0 = 1.492$, $C_1 = 0.0847$, $C_2 = -0.0211$, $C_3 = -0.0004$ achieving an R^2 of 1. Doping significantly influences the relative stability and alters both the electronic and magnetic properties of the material. The correlation between overpotential and these properties, as outlined in eqn (12), can be articulated as follows: the Mulliken spin population analysis, summarized in Table S5,† reveals a reduction in spin density when the endohedral Cu-atom is substituted with other transition metals (TM). Fig. 7 illustrates

a linear decrease in the overpotential for the CO_2 to CO reduction, establishing a direct correlation between magnetism and catalytic activity. Furthermore, the variation in polarizability arises from changes in electronic properties, which are intrinsically linked to the equilibrium structure, as evidenced by Fig. 1 and 2. This study highlights the dependence of overpotentials on the interplay between magnetism, equilibrium structures, and electronic properties.

4. Conclusion

In this study, we have systematically investigated the equilibrium structures, electronic and magnetic properties of transition metal atom-doped icosahedral copper clusters, XCu_{12} (X = 3d and 4d transition metal atoms), using a multi-scale theoretical approach that combines the artificial bee colony algorithm, the extended tight binding model, and density functional theory (DFT). Our findings reveal that doping significantly influences their electronic configurations, magnetic properties, and stability. In addition, Transition metal-doped Cu12 clusters exhibit an enhanced ability to bind, activate, and electrochemically reduce CO_2.

Among the clusters studied, $CrCu_{12}$ and $MoCu_{12}$ stand out as the most stable clusters among the 3d and 4d series, respectively, due to their closed electronic shell structures. This shell closing also leads to quenched magnetic moments even though Cr and Mo possess the highest magnetic moments in their respective series. While closed-shell systems should be relatively chemically inert, $CrCu_{12}$ and $MoCu_{12}$ can bind and activate CO_2. The findings further reveal a direct correlation between the electronic and magnetic properties of the clusters and their catalytic performance, with transition metal-doped clusters exhibiting approximately a 20% decrease in overpotential for CO_2 reduction compared to the pure Cu_{13} cluster. The proposed empirical formula based on DFT data further enhances our ability to predict the properties of similar clusters, providing a valuable tool for future material design.

Data availability

The data supporting this article have been included as part of the ESI.†

Conflicts of interest

There are no conflicts of interest to declare.

Acknowledgements

MKM and PJ acknowledge financial support from the U.S. Department of Energy, Office of Basic Energy Sciences, Division of Materials Sciences and Engineering under Award No. DE-FG02-96ER45579. Resources of the National Energy Research Scientific Computing (NERSC) Center supported by the Office of Science of the U.S. Department of Energy under Contract No. DE-AC02-05CH11231 is also acknowledged. The authors extend their acknowledgment to the High-Performance Research Computing (HPRC) core facility at Virginia Commonwealth University for providing supercomputing resources.

References

1 M. González-Castaño, B. Dorneanu and H. Arellano-García, *React. Chem. Eng.*, 2021, **6**, 954–976.
2 P. Huang, J. Huang, J. Li, T. D. Pham, L. Zhang, J. He, G. W. Brudvig, N. A. Deskins, A. I. Frenkel and G. Li, *J. Phys. Chem. C*, 2022, **126**, 8596–8604.
3 E. V. Kondratenko, G. Mul, J. Baltrusaitis, G. O. Larrazábal and J. Pérez-Ramírez, *Energy Environ. Sci.*, 2013, **6**, 3112–3135.
4 A. Vasileff, Y. Zheng and S. Z. Qiao, *Adv. Energy Mater.*, 2017, **7**, 1700759.
5 W. Zhu, R. Michalsky, Ö. Metin, H. Lv, S. Guo, C. J. Wright, X. Sun, A. A. Peterson and S. Sun, *J. Am. Chem. Soc.*, 2013, **135**, 16833–16836.
6 G. Zhang, L. Li, Z.-J. Zhao, T. Wang and J. Gong, *Acc. Mater. Res.*, 2023, **4**, 212–222.
7 Z. Han, D. Han, Z. Chen, J. Gao, G. Jiang, X. Wang, S. Lyu, Y. Guo, C. Geng, L. Yin, Z. Weng and Q.-H. Yang, *Nat. Commun.*, 2022, **13**, 3158.
8 K. P. Kuhl, E. R. Cave, D. N. Abram and T. F. Jaramillo, *Energy Environ. Sci.*, 2012, **5**, 7050–7059.
9 X. Chen, J. Chen, N. M. Alghoraibi, D. A. Henckel, R. Zhang, U. O. Nwabara, K. E. Madsen, P. J. A. Kenis, S. C. Zimmerman and A. A. Gewirth, *Nat. Catal.*, 2021, **4**, 20–27.
10 B. Yang, C. Liu, A. Halder, E. C. Tyo, A. B. F. Martinson, S. Seifert, P. Zapol, L. A. Curtiss and S. Vajda, *J. Phys. Chem. C*, 2017, **121**, 10406–10412.
11 C. Liu, B. Yang, E. Tyo, S. Seifert, J. DeBartolo, B. von Issendorff, P. Zapol, S. Vajda and L. A. Curtiss, *J. Am. Chem. Soc.*, 2015, **137**, 8676–8679.
12 Q.-Y. Fan, Y. Wang and J. Cheng, *J. Phys. Chem. Lett.*, 2021, **12**, 3891–3897.
13 A. Ma, Y. Ren, Y. Zuo, J. Wang, S. Huang, X. Ma and S. Wang, *Chem. Commun.*, 2024, **60**, 3162–3165.
14 T. Kawawaki, T. Okada, D. Hirayama and Y. Negishi, *Green Chem.*, 2024, **26**, 122–163.
15 L.-J. Liu, Z.-Y. Wang, Z.-Y. Wang, R. Wang, S.-Q. Zang and T. C. W. Mak, *Angew. Chem., Int. Ed.*, 2022, **61**, e202205626.
16 C. Liu, H. He, P. Zapol and L. A. Curtiss, *Phys. Chem. Chem. Phys.*, 2014, **16**, 26584–26599.
17 Y. Gao, N. Shao, S. Bulusu and X. C. Zeng, *J. Phys. Chem. C*, 2008, **112**, 8234–8238.
18 F. Mehmood, J. Greeley and L. A. Curtiss, *J. Phys. Chem. C*, 2009, **113**, 21789–21796.
19 B. Barhács, E. Janssens and T. Höltzl, *Phys. Chem. Chem. Phys.*, 2022, **24**, 21417–21426.

20 L. Jin-Cheng, X. Hai, Z. Xiao-Kun, Z. Nan-Nan, L. Yuan, X. Deng-Hui, Y. Xiaohu, H. Han-Shi and L. Jun, *CCS Chem.*, 2022, **5**, 152–163.
21 Y. Pan, H. Li, J. Xiong, Y. Yu, H. Du, S. Li, Z. Wu, S. Li, J. Lai and L. Wang, *Appl. Catal., B*, 2022, **306**, 121111.
22 D.-H. Nam, O. S. Bushuyev, J. Li, P. De Luna, A. Seifitokaldani, C.-T. Dinh, F. P. García de Arquer, Y. Wang, Z. Liang, A. H. Proppe, C. S. Tan, P. Todorović, O. Shekhah, C. M. Gabardo, J. W. Jo, J. Choi, M.-J. Choi, S.-W. Baek, J. Kim, D. Sinton, S. O. Kelley, M. Eddaoudi and E. H. Sargent, *J. Am. Chem. Soc.*, 2018, **140**, 11378–11386.
23 D. Yang, S. Zuo, H. Yang, Y. Zhou, Q. Lu and X. Wang, *Adv. Mater.*, 2022, **34**, 2107293.
24 S. Zhang, L. Chen, X. S. Luan and H. Li, *Chem. Phys.*, 2022, **557**, 111487.
25 Z. Zhao, Z. Chen, X. Zhang and G. Lu, *J. Phys. Chem. C*, 2016, **120**, 28125–28130.
26 M. Ma, K. Djanashvili and W. A. Smith, *Angew. Chem., Int. Ed.*, 2016, **55**, 6680–6684.
27 P. Hirunsit, *J. Phys. Chem. C*, 2013, **117**, 8262–8268.
28 H. Tao, Y. Li, X. Cai, H. Zhou, Y. Li, W. Lin, S. Huang, K. Ding, W. Chen and Y. Zhang, *J. Phys. Chem. C*, 2019, **123**, 24118–24132.
29 L.-X. Ran, D.-W. Deng, Y.-B. Li, Q.-X. Ge, J. Wu, X.-B. Li, Z.-K. Tang and W.-J. Yin, *J. Phys. Chem. C*, 2024, **128**, 13464–13472.
30 N. N. Ha, N. T. T. Ha and L. M. Cam, *J. Mol. Graphics Modell.*, 2021, **107**, 107979.
31 S. K. Iyemperumal and N. A. Deskins, *Phys. Chem. Chem. Phys.*, 2017, **19**, 28788–28807.
32 R. P. B. Silalahi, K. K. Chakrahari, J.-H. Liao, S. Kahlal, Y.-C. Liu, M.-H. Chiang, J.-Y. Saillard and C. W. Liu, *Chem. – Asian J.*, 2018, **13**, 500–504.
33 J. Zhang and M. Dolg, *Phys. Chem. Chem. Phys.*, 2015, **17**, 24173–24181.
34 J. Zhang and M. Dolg, *Phys. Chem. Chem. Phys.*, 2016, **18**, 3003–3010.
35 A. D. Becke, *J. Chem. Phys.*, 1992, **97**, 9173–9177.
36 A. D. Becke, *J. Chem. Phys.*, 1993, **98**, 5648–5652.
37 B. P. Pritchard, D. Altarawy, B. Didier, T. D. Gibson and T. L. Windus, *J. Chem. Inf. Model.*, 2019, **59**, 4814–4820.
38 M. Frisch, G. Trucks, H. Schlegel, G. Scuseria, Ma. Robb, J. Cheeseman, G. Scalmani, V. Barone, G. Petersson and H. Nakatsuji, *Gaussian 16, Revision A. 03*, Gaussian, Inc., Wallingford CT, 2016.
39 S. Grimme, J. Antony, S. Ehrlich and H. Krieg, *J. Chem. Phys.*, 2010, **132**, 154104.
40 T. Lu and F. Chen, *J. Comput. Chem.*, 2012, **33**, 580–592.
41 G. Kresse and J. Furthmüller, *Phys. Rev. B:Condens. Matter Mater. Phys.*, 1996, **54**, 11169–11186.
42 G. Kresse and J. Furthmüller, *Comput. Mater. Sci.*, 1996, **6**, 15–50.
43 J. P. Perdew, K. Burke and M. Ernzerhof, *Phys. Rev. Lett.*, 1996, **77**, 3865–3868.
44 P. E. Blöchl, *Phys. Rev. B:Condens. Matter Mater. Phys.*, 1994, **50**, 17953–17979.
45 Data repository, **https://github.com/manishkmr484/Cluster_Geom**.
46 A. Muthuperiyanayagam, A. G. Nabi, Q. Zhao, Aman-ur-Rehman and D. Di Tommaso, *Phys. Chem. Chem. Phys.*, 2023, **25**, 13429–13441.
47 Q. Zhang and L. Guo, *J. Cluster Sci.*, 2018, **29**, 867–877.
48 N. Kuganathan, E. N. Sgourou, A. Chroneos and C. A. Londos, *Physica B: Condens. Matter*, 2024, **674**, 415540.
49 Q. Sun, X. G. Gong, Q. Q. Zheng, D. Y. Sun and G. H. Wang, *Phys. Rev. B:Condens. Matter Mater. Phys.*, 1996, **54**, 10896–10904.
50 Quantum cluster database.
51 G. Zhu, Y. Li, H. Zhu, H. Su, S. H. Chan and Q. Sun, *ACS Catal.*, 2016, **6**, 6294–6301.
52 M. E. Kilic and P. Jena, *J. Phys. Chem. Lett.*, 2023, **14**, 8697–8701.
53 Megha, K. Mondal, T. K. Ghanty and A. Banerjee, *J. Phys. Chem. A*, 2021, **125**, 2558–2572.
54 B.-W. Tang, Y. Liu, D.-W. Deng, Y. Xu, B. Wen, Z.-K. Tang, X.-L. Wei, Q.-X. Ge and W.-J. Yin, *Phys. Chem. Chem. Phys.*, 2022, **24**, 26556–26563.
55 J. K. Nørskov, J. Rossmeisl, A. Logadottir, L. Lindqvist, J. R. Kitchin, T. Bligaard and H. Jónsson, *J. Phys. Chem. B*, 2004, **108**, 17886–17892.
56 A. A. Peterson, F. Abild-Pedersen, F. Studt, J. Rossmeisl and J. K. Nørskov, *Energy Environ. Sci.*, 2010, **3**, 1311–1315.
57 S. Baskaran and J. Jung, *Appl. Surf. Sci.*, 2022, **592**, 153339.
58 J. Nakamura, J. M. Campbell and C. T. Campbell, *J. Chem. Soc., Faraday Trans.*, 1990, **86**, 2725–2734.
59 L. Chen, Q. Zhang, Y. Zhang, W. Z. Li, B. Han, C. Zhou, J. Wu, R. C. Forrey, D. Garg and H. Cheng, *Phys. Chem. Chem. Phys.*, 2010, **12**, 9845–9851.
60 L. Gong, X. Wang, T. Zheng, J. Liu, J. Wang, Y.-C. Yang, J. Zhang, X. Han, L. Zhang and Z. Xia, *J. Mater. Chem. A*, 2021, **9**, 3555–3566.
61 E. Clementi, D. L. Raimondi and W. P. Reinhardt, *J. Chem. Phys.*, 1967, **47**, 1300–1307.